Split Control Wind Turbine Airfoil noise with CFD and Acoustic Analogies

S. Khenfous[1†], M. Maizi[2] and M. Zamoum[3]

[1] *Research Laboratory LRME, Department of Physics, Faculty of Sciences, M'Hamed Bougara University of Boumerdes, Boumerdes, 35000, Algeria*
[2] *Renewable Energy Development Center, Bouzareah, Algiers, 16340, Algeria*
[3] *Laboratory of Hydrocarbons Physical Engineering, LGPH Faculty of Sciences,M'Hamed Bougara University of Boumerdes, 35000, Boumerdes, Algeria*

[†] *Corresponding Author Email: s.khenfous@univ-boumerdes.dz*

ABSTRACT

This research aims to investigate the impact of a split airfoil on noise emissions from a horizontal-axis wind turbine. The objective is to comprehensively understand the airflow patterns around the airfoil to reduce noise emissions. The study rigorously examines a range of angles of attack, from 0° to 25°, for both the original airfoil and the airfoil with a split, using advanced computational aerodynamics coupled with analog acoustic analysis. The methodology involves two-dimensional flow simulations with Delayed Detached Eddy Simulation based on the Spalart-Allmaras model, enabling precise near-field flow calculations around the airfoil. Additionally, far-field noise predictions, employing the Ffowcs Williams and Hawkings analogy based on simulated sources, reveal the efficacy of the split airfoil design. Results indicate that the split airfoil design effectively reduces noise emissions across various angles of attack. These reductions translate into a significant decrease in the Overall Sound Pressure Level, ranging from 14% to 19%, and remarkable Sound Pressure Level reductions between 12% and 60% across diverse frequencies, showcasing substantial noise improvements in various frequency ranges.

1. INTRODUCTION

The challenges posed by overconsumption, escalating energy demand, and the depletion of fossil fuel reserves are critical for humanity. Consequently, there has been a global shift towards alternative energy sources as optimal and efficient solutions. Wind energy emerges as a notable contributor to contemporary electricity production (Ackermann & Söder, 2000). Over the past two decades, various studies and efforts have been undertaken to enhance the quality of wind power generation. Nevertheless, significant impediments persist, particularly in the realm of noise, hindering its widespread adoption (Mohamed, 2019).

Wind turbine noise, categorized into aerodynamic and mechanical types, presents a significant concern. Mechanical noise originates from component mechanisms, while aerodynamic noise results from the airflow around the blades (Liu, 2017). The latter is further divided into tonal noise, associated with low frequencies linked to blade rotation, and broadband noise, arising from the interaction between atmospheric turbulence and turbine blades (Anicic et al., 2016; Maizi et al., 2018).

Numerical simulations offer a valuable tool for investigating noise generation and propagation. However, conducting direct calculations for intricate industrial geometries to simultaneously analyze aerodynamic and acoustic fields remains challenging. Coupled methods, such as CFD with acoustic analog, emerge as the most viable approach for predicting noise propagation in the far field. Numerous studies, encompassing experimental, numerical, and analytical approaches, have been undertaken to advance the understanding and prediction of aerodynamic noise (Mo & Lee, 2011; Mohamed, 2014; Wasala et al., 2015; Luo al., 2015).

The research conducted by Wasala et al. (2015), centers on investigating wind turbine-generated noise using Large Eddy Simulation (LES) within a confined computational domain, targeting a blade area recognized for substantial noise generation. Utilizing the Ffowcs-

Williams and Hawkings (FW–H) acoustic analogy, their study reliably forecasts far-field sound. Notably, the numerical outcomes for the CART-2 wind turbine closely align with experimental data.

A computational framework considering the actual wind turbine blade geometry was developed by Luo et al. (2015), to accurately compute aerodynamics and aeroacoustics. In general, the LES simulation results demonstrated favorable alignment with the experimental data. The study delved into the formation of complex 3D wake vortices and their relationship to aerodynamic noise using the FW-H method. It revealed that noise generation was linked to the evolution of these vortices, particularly originating from the blade tip region.

To simulate the aeroacoustic noise produced by the NREL phase 5 wind turbine, Mo and Lee (2011), implemented a hybrid methodology merging an LES model with an acoustic analog. Their outcomes established a clear and substantial relationship between escalating wind speeds and the production of quadrupole-type noise across varying structural dimensions.

Mohamed's (2014) study investigated the Darrieus turbine's aero-acoustics, focusing on the noise generated by its blades. Using FWeH equations, the study explored the impacts of solidity, tip speed ratio, and blade form. Results showed a positive correlation between higher tip speed ratios and increased turbine noise.

As previously indicated, noise significantly impairs the efficient utilization of wind energy. Consequently, researchers are actively exploring methodologies to enhance flow behavior around wind turbine blades by implementing passive and/or active flow control techniques. Passive control, being cost-effective and straightforward without requiring supplementary energy, stands as the most extensively employed approach. Numerous investigations have scrutinized the influence of diverse passive control methods on the aerodynamic performance of wind turbine blades, encompassing gurney flaps, vortex generators, dimples, micro-cylinders, and other innovative airfoil designs. Mohamed (2021) mitigated the aerodynamic noise generated by small vertical axis wind turbines by substituting the typical single-rotor Darrieus turbine with three rotors of the same frontal area. The numerical investigation of various geometric and operating conditions revealed that, despite a 3.1% average reduction in power coefficient, this alteration significantly decreased aerodynamic noise by 43%.

Maizi et al. (2017) demonstrated in their study the potential to reduce noise levels by adjusting the pitch angle without significantly sacrificing power output. Employing three-dimensional flow simulations, including two unsteady computational fluid dynamics (CFD) methods—URANS and DES—the study assesses the near-field flow around a small-scale NREL Phase VI HAWT. And the predictions of far-field noise using the Ffowcs Williams and Hawkings analogy are compared with measured noise levels, revealing a generally good agreement, especially for DES predictions. Additionally, in 2018, Maizi et al. conducted an investigation into the influence of blade tip shape on noise emissions from horizontal axis wind turbines (HAWTs). They tested three different tip blade configurations using computational methods. The results of their study demonstrate that a specific tip shape has a significant impact on noise emission, particularly in the high-frequency range, offering the potential to reduce sound pressure levels.

To investigate the impact of blade splitting along the span of a HAWT blade, Moshfeghi et al. (2017) conducted both 2D and 3D simulations on a S809 airfoil. It assessed various split configurations and different tip speed ratios at constant rotational speed. The findings highlighted significant torque sensitivity to split location and flow angle for attached flow conditions, while the aerodynamic performance of the blade was less affected by split location during strongly separated flow within the turbine. Recently, a study to investigate the effects of the radial split position of five different versions of NREL Phase VI and original blade was performed also by Moshfeghi and Hur (2020). The results of CFD simulations demonstrate that the power generated by the split blades at any tip speed ratios less than 3.5 and for blade in which the split extends from the blade root to the blade tip at a stall condition is higher than the No split blade power generation. Additionally, Moshfeghi et al. (2021) presented the effectiveness of a double-split configuration, using an unsteady DES simulation of both 3D single and double splits of S809 airfoil profile. It was determined that at 17°<AOA<22° the double-split model showed the highest performance contrary of the configuration at 0°<AOA<17° which had the poorest performance.

With a view to controlling the flow around a NACA 4412 airfoil by increasing lift and decreasing drag, Beyhaghi & Amano (2017) proposed to drill a narrow span-wide slot near the leading edge of the airfoil, several combinations of slot geometrical parameters were tested under different angles of attack to determine the

optimal configurations. Indeed, the authors found that an average improvement of 8% is observed for the lift coefficient over the entire AOA range (with the maximum increase of 15% for AOA=0), without any significant drag penalty. In 2018, a supplementary study of this research was done by Beyhaghi and Amano (2018), using computational investigations for modeling and analysis, and a series of wind tunnel experiments for validation. The results reveal that for one of the best cases examined, a lift coefficient improvement as large as 30% is observed, while the drag penalty is insignificant.

A Computational Fluid Dynamics (CFD) simulations are employed on the DU12W262 airfoil to shed light on the impact of the combination of splits with a flexible slot shape parameterization coupled with an optimizer on horizontal and vertical axis wind turbines by Acarer (2020), the results show that the concept is highly successful in improving peak and overall CL/CD of the airfoil, and this yields to significant enhancements in both HAWTs and VAWTs.

Previous research on split blades has largely focused on the aerodynamic performance of this configuration, often neglecting its impact on noise emission. In contrast, our study breaks new ground by conducting a comprehensive assessment of the radiated noise originating from the S809 airfoil with and without a split. This novel focus on the acoustic aspect of split airfoils fills a significant gap in the current body of research.

To achieve this, we employ a combined approach using Detached Eddy Simulation (DDES) with the Spalart-Allmaras method, integrated with the Ffowcs Williams-Hawkings analogy to simultaneously compute both aeroacoustic and aerodynamic fields. This multidisciplinary approach allows for a more holistic analysis of the interplay between aerodynamic performance and noise emission.

By providing a detailed investigation into how the use of a split airfoil affects noise characteristics, our study offers new insights that could inform future designs and applications in various fields such as aerospace and wind energy. Our findings could pave the way for innovations that optimize both aerodynamic performance and noise reduction in airfoil design.

2. METHODOLOGY

2.1 Delayed Detached Eddy Simulation

In this investigation, the chosen turbulence model is the Delayed Detached Eddy Simulation (DDES) with the Spalart-Allmaras model. This model derives its foundations from the Detached Eddy Simulation (DES) method, originally proposed by Spalart in 1994. DES represents a hybrid approach that amalgamates the advantages of both Reynolds-Averaged Navier-Stokes (RANS) and Large Eddy Simulation (LES) turbulence models. Within the DES framework, the unsteady RANS model is applied to address the boundary layer, while LES is employed in regions where flow separation occurs. DES adapts its behavior based on local grid

spacing and the computed turbulent length scale derived from the turbulence model. When the mesh and grid spacing reach a level of precision finer than the turbulent length scale, the DES model shifts into LES mode. It is worth noting that DES strikes a balance between computational cost, falling between the more computationally intensive LES and the less intensive RANS models (Spalart, 2000; Spalart et al., 2006; Maizi et al. 2017; Liu et al., 2019).

The Spalart-Allmaras model is a single-equation model designed to solve a transport equation representing kinematic eddy viscosity. In ANSYS Fluent, the Spalart-Allmaras model has been enhanced with a Y+ insensitive wall treatment, enabling its application regardless of the near-wall Y+ resolution. This enhancement allows for an automatic transition from a viscous sublayer formulation to a logarithmic formulation based on Y+. Consequently, when employing the Spalart-Allmaras turbulence model, it does not necessitate an overly fine grid near the wall, merely a grid equivalent to the desired algebraic turbulence model. Consequently, it has the advantage of being simple to calculate and has a rapid convergence speed for simple flows (Spalart & Allmaras, 1992; Liu et al., 2019).

2.2 Acoustic Analogy Method

The acoustic analogy developed by Ffowcs Williams and Hawkings, based on Lighthill's acoustic analogy (Lighthill, 1952), is a method designed for simulating the acoustic radiation generated by arbitrarily moving surfaces in the far field. This technique relies on analytically calculated integral solutions to wave equations. The near-field flow, derived from appropriate governing equations like unsteady RANS equations, DES, or LES, is used to predict sound propagation. Importantly, this acoustic analogy effectively separates sound transmission from sound generation, enabling the flow solution process to be distinct from acoustic analysis (Williams & Hawkings, 1969; Su, et al. 2019). The FW-H equation essentially represents a non-homogeneous wave equation derived through manipulations of the continuity equation and the Navier-Stokes equations (Brentner & Farassat, 1998; Maizi et al., 2017). It can be written as (Williams & Hawkings, 1969):

$$\frac{1}{a_0^2}\frac{\partial^2 p'}{\partial t^2} - \nabla^2 p' = \frac{\partial^2}{\partial x_i \partial x_j}\left[T_{ij}H(f)\right]$$

$$-\frac{\partial}{\partial x_i}\left[\left(P_{ij}n_j + \rho u_i(u_n - v_n)\right)\delta(f)\right]$$

$$+ \frac{\partial}{\partial t}\left[\left(\rho_0 v_n + \rho(u_n - v_n)\right)\delta(f)\right] \quad (1)$$

Where the first term on the right side represents a quadruple source due to unsteady shear stresses, the second term is a dipole source caused by unsteady external forces, and the third term is a monopole source resulting from unsteady mass injection. Here, u_i and v_i are the respective fluid and surface velocity components in the x_i direction, u_n and v_n are the respective fluid and surface velocity components normal to the surface. $\delta(f)$ represents the Dirac delta function, and H(f) is the Heaviside function. P_{ij} represents the compressive stress
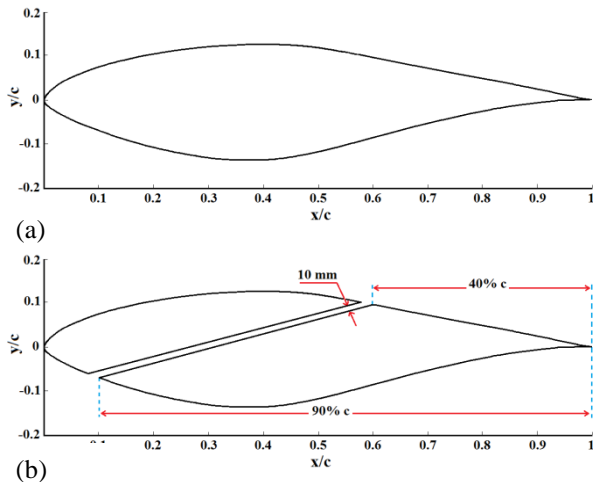
Fig. 1 S809 NREL airfoil: (a) Original airfoil (b) Split airfoil configuration

tensor, and p' is the sound pressure in the far field. The notation (f = 0) indicates a mathematical surface introduced to surround the exterior flow problem (f > 0) in an unbounded space. This mathematical surface aids in applying a generalized theory and the free-space Green equation to obtain the solution.

The surface (f = 0) represents the source (emission) surface, which includes the blade and shaft. The unit normal vector, n_j, points towards the exterior region (f > 0). The parameter a_0 denotes the far-field sound speed, and T_{ij} refers to the Lighthill stress tensor (Mo & Lee, 2011; Ansys, 2013), as defined in Eq. (2):

$$T_{ij} = \rho\, u_i u_j + P_{ij} - a_0^2 (\rho - \rho_0)\delta_{ij} \qquad (2)$$

Sound pressure signals at the specified receiver locations are computed using the source data collected during the aerodynamic simulations and converted to the frequency domain using the Fast Fourier transform algorithm. The following formula is used to calculate the sound pressure level (SPL) (Ansys, 2013):

$$SPL(dB) = 10\log_{10}\left(\frac{PSD}{P_{ref}}\right) \qquad (3)$$

Within the framework of acoustic analysis, the variable *PSD* signifies the Power Spectral Density for either a particular Fourier mode or a particular frequency band. Concurrently, P_{ref} denotes the auditory threshold for the human ear, a precisely defined quantity resting at 2.10^{-5} Pa. In the pursuit of precise acoustic quantification, these methodologies excel at yielding significant measurements of acoustic noise intensity. The overall sound pressure level (*OASPL*) is one such metric, and it is defined as follows:

$$OASPL(dB) = 10\log_{10}\left(\sum_{i=1}^{n} 10^{\frac{SPL(i)}{10}}\right) \qquad (4)$$

Here, *SPL(i)* represents the octave band sound pressure level in the broadband frequency domain, and 'n' stands for the total number of octave bands spanning from the lowest to the highest concerned frequencies.

3. METHODOLOGY

3.1 Mesh topology and boundary conditions

The objective of this research is twofold: firstly, to predict the aerodynamic noise generated by a horizontal wind turbine airfoil and, secondly, to explore how the implementation of a split airfoil affects this noise. For our analysis, we have selected the S809 NREL airfoil (Fig. 1), primarily because it offers readily available numerical and experimental data for validation purposes, as highlighted by (Somers, 1997). In addition to simulating the original airfoil configuration, we have also incorporated the splitting technique as a passive control method. The parameters for the split airfoil in this study are derived from the work of Moshfeghi et al. (2017. Specifically, we have implemented the split by separating the suction and pressure surfaces from the trailing edge at 40% and 90% of the chord length, respectively, as in Fig. 1. Furthermore, we have maintained a consistent split width of 10 mm, well within the effective range for split width, across the blade span.

To ensure both result accuracy and computational efficiency, a high-quality mesh is imperative. As depicted in Fig. 2, this study adopted a hybrid grid generated using the ANSYS ICEM pre-processor. The airfoil is positioned at the center of a C-type grid, encompassed by a semicircular region with a radius of 20*c, and a rectangular area measuring 40*c in length and 20*c in width located at the backside.
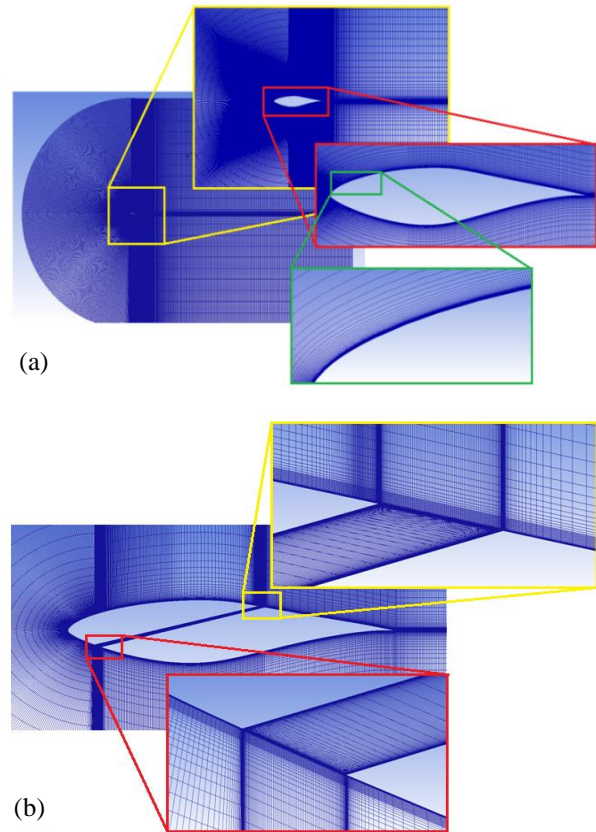

Fig. 2 Computational meshes for different airfoils: (a) Original airfoil meshes (b) Split airfoil meshes
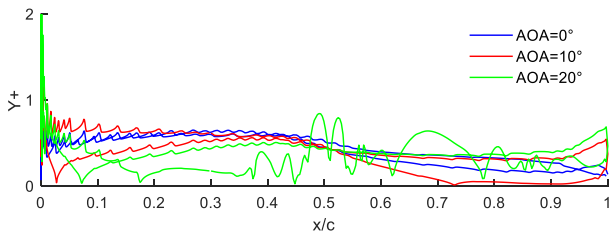
Fig. 3 S809 airfoil Y+ distribution for AOA values of 0°, 10°, and 20°

The domain was discretized using structured quadrilateral cells, with finer mesh near the airfoil gradually transitioning to coarser mesh as the distance from the airfoil increased. An inflation layer was implemented around the airfoil to precisely capture boundary layer effects. The first row of cells adjacent to the airfoil was set to a height of 10^{-5} meters, ensuring a y^+ value of approximately 1 (refer to Fig. 3).

For boundary conditions, the airfoil was treated as a no-slip wall. Inlet boundary conditions were defined with velocities $u = V \cos(\alpha)$, $v = V \sin(\alpha)$, and $w = 0$, where $V = 30.9$ [m.s^{-1}] represents the average wind velocity, and α is the angle of attack. The air was assumed to have a density of 1.185 [kg.m^{-3}] and a viscosity of 1.831e^{-05} [kg.m^{-1}.s^{-1}]. The pressure outlet was set to 0 [Pa].

3.2 Mesh Independence Study

Due to the substantial influence of mesh quality on the results, performing a mesh independence test is a crucial step in the simulation process. This test aims to determine the optimal number of cells in the computational domain, striking a balance between result accuracy and computational efficiency. In our study, we systematically refined mesh sizes, assessing the impact on the lift coefficient until any further adjustments yielded negligible changes.

Figure 4 illustrates the lift coefficient of the airfoil at an angle of attack of 8° for seven different mesh element counts. Our analysis indicates that 360,000 elements provide a satisfactory grid size, delivering a favorable compromise between result precision and computational resources. This mesh size of 360,000 elements is subsequently adopted for all simulations involving the original airfoil. However, it's important to note that the
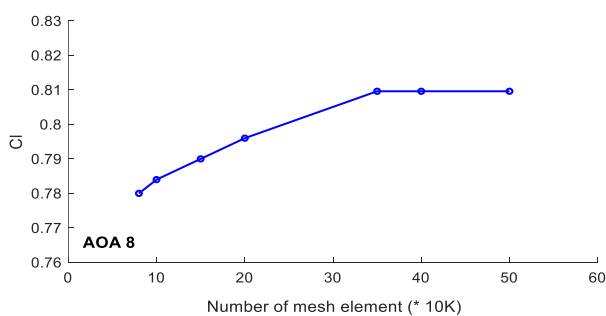
element count increases to 390,000 for airfoils with a split configuration.

3.3 Solver Sittings

All simulations in this research were conducted using the commercial CFD solver ANSYS Fluent, which is based on the finite volume approach to solving the Navier-Stokes equations. Transient 2D simulations were performed using the Delayed Detached Eddy Simulation (DDES) with the Spalart-Allmaras model. Given that Mach numbers based on blade tip speed never exceeded 0.3, the flow around the wind turbines can be considered essentially incompressible.

The discretization methods employed were second order for pressure and bounded central differencing for momentum. Pressure-velocity coupling was achieved using the COUPLED scheme, and a second-order implicit scheme was employed for time integration. To accurately capture acoustic signals with significantly smaller amplitudes compared to flow fluctuations, a time step of 5.10^{-5} seconds was chosen, allowing for noise spectrum calculation up to 10 kHz frequency.

Convergence criteria were set for each time step, with a scaled residual of 10^{-4} applied to the continuity equation and each directional component of velocity. Typically, convergence was achieved in less than 20 iterations per time step.

To attain a statistically steady-state solution, a total of 10,000 time steps were employed for each case. The "Compute Acoustic Signals Simultaneously" option was utilized to compute sound pressure signals concurrently with the transient flow solution, eliminating the need to save source data.

A comprehensive analysis employed a total of 144 receivers. As depicted in the Fig. 5, thirty-six receivers were evenly distributed at ten-degree intervals in a circular pattern. Additionally, an average of four receivers was strategically placed at varying distances from the airfoil, specifically at 2c, 4c, 6c, and 10c, where "c" represents the chord length.

Fig. 4 Grid independence study for the S809 airfoil CFD simulation: Lift Coefficient at 8° angle of attack for different grid numbers
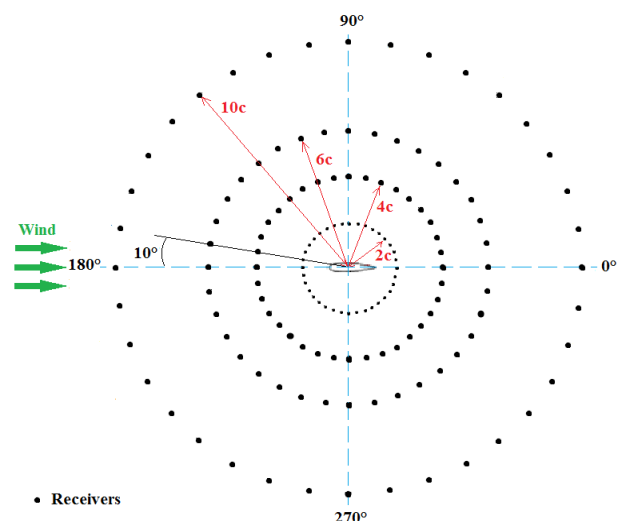

Fig. 5 Receiver distribution pattern for comprehensive acoustic analysis around the Airfoil
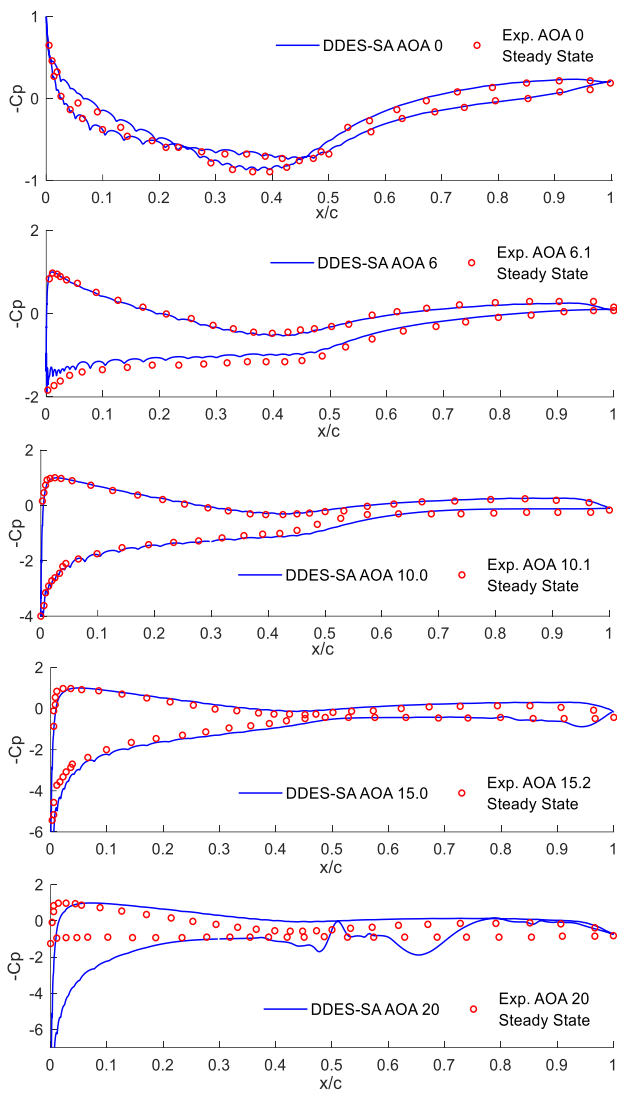
Fig. 6 Comparison between experimental and numerical pressure coefficient distributions at different angles of attack

4. RESULTS

4.1 Aerodynamic Validation

The validity of the numerical turbulence model used in this study was established through a comparison of pressure coefficients with experimental data collected by Somers, 1997. These experiments were conducted in the low-turbulence wind tunnel of the Low-Speed Laboratory at Delft University of Technology (DUT) in the Netherlands. The formula below is employed for calculating the pressure coefficient (Cp):

$$C_p = \frac{p - p_\infty}{\frac{1}{2}\rho V^2} \tag{5}$$

Where, p is the local pressure, p_∞ represents the ambient pressure which is equal to 1.01325 [kPa] and ρ is the density of air.

The pressure coefficients corresponding to five discrete angles of attack, specifically 0°, 6°, 10°, 15°, and 20°, at a Reynolds number of 1.10^6, are graphically presented in Fig. 6. It is discernible that, irrespective of the angle of attack, the pressure distributions on both the upper and lower surfaces of the airfoil exhibit a substantial congruence with experimental data.

4.2 Aeroacoustic Validation

Regrettably, there is an absence of available experimental aeroacoustic data for the S809 airfoil to validate the results of acoustic simulations.

Consequently, to ensure the accuracy and reliability of the computational aeroacoustic method, we initially applied it to analyze the DU96 airfoil. We validated the method by comparing our results to the acoustic experimental measurements from Devenport et al. (2010). This comparison was essential for confirming the method's precision and consistency by evaluating how closely the simulation aligned with the experimental data. Once we established confidence in the method's reliability with the DU96 airfoil, we used it to simulate the S809 airfoil. This approach provided a robust basis for accurately evaluating the S809 airfoil's acoustic and aerodynamic performance.

Figure 7 presents a comparison between the Sound Pressure Level derived from simulation data and experimental measurements for the DU96 airfoil. Under identical flow conditions at AOA=6° and Re=3,200,000, this comparison reveals a pronounced resemblance between the results and experimental data.

The acoustic pressure level results from the DES model are very close to the experimental data, mostly for the whole range of frequencies below 3000 Hz. The findings reveal that the difference in SPL between numerical predictions and experimental measurements was within ± 5 dB for frequencies below 1000 Hz. Notably, the noise radiation is almost superimposed for frequencies below 3000 Hz in experimental values. Based on these outcomes, we can confidently recommend the utilization of a DES model and the same simulation methodology for predicting S809 airfoil noise emission.

4.3 The Impact of Receiver Distance and Angle of Attack on Noise Levels

The relationship between sound intensity and the distance from the sound source to the receiver is a fundamental principle in acoustics. This concept is
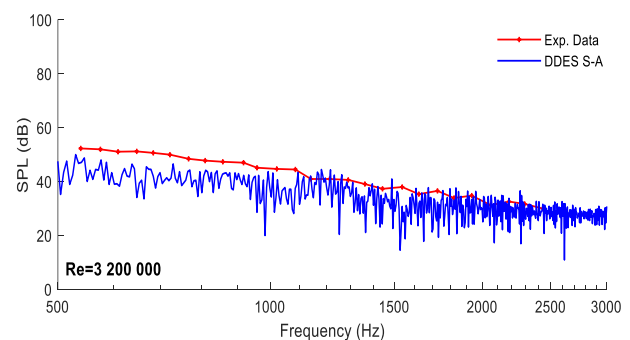

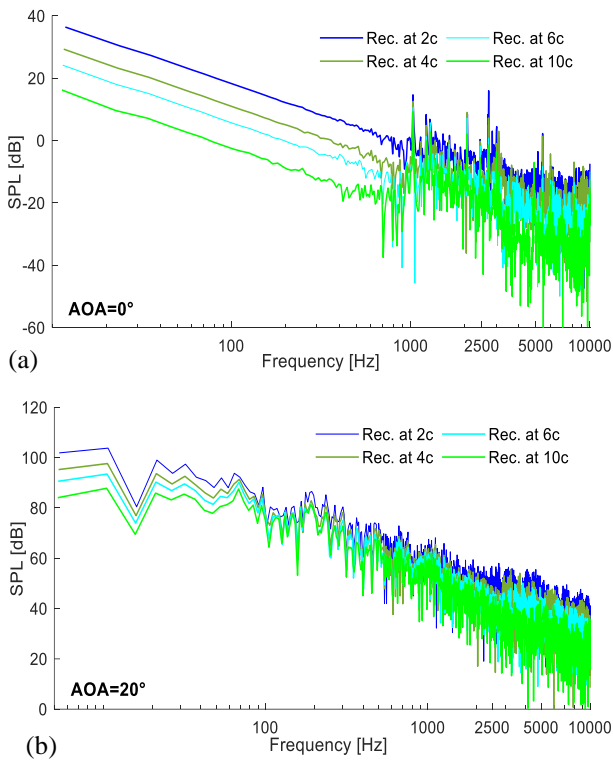**Fig. 7 Sound Pressure Levels of simulation and experimental data for DU96 Airfoil**

Fig. 8 Sound pressure level spectra at different receiver distances for: (a) AOA= 0° (b) AOA= 20°

exemplified in Fig. 8 and Fig. 9, where the established direct proportionality is visually demonstrated.

Figure 8 specifically illustrates the impact of distance on sound pressure levels in the vertical direction at two angles of attack. This is achieved by calculating Sound Pressure Level (SPL) at various distances from the airfoil (2c, 4c, 6c, and 10c). Notably, all the spectra for different distances exhibit consistent behavior with

identical tonal peak positions. Moreover, it is evident that the sound pressure level decreases as the distance between the receiver and the airfoil increases.

In order to delineate the OASPL curves, a total of 144 receivers were employed, as previously indicated in the 'Solver Settings' section. Twenty-five simulations, each encompassing 10,000 time steps, were executed to calculate the power spectral density. Following this, a manual analysis of the outcomes was conducted prior to undertaking the calculation and plotting of the OASPL curves. This process was accomplished using the MATLAB software, incorporating an algorithm developed by our team.

The same can be observed in Fig. 9 which provides a representation of how distance affects the overall sound pressure level (OASPL) for two angles of attack (AOA=0° and AOA=20°). Particularly in the vertical direction (with receivers at 90°), it's worth noting that at AOA=0°, there is a noticeable increase of 6.81 dB when transitioning from 2c to 4c. This is followed by a 4.7 dB increase from 4c to 6c and a subsequent 6 dB increase from 6c to 10c. Similarly, at AOA=20°, a 4.4 dB increase is observed at 2c compared to 4c, along with a 2.6 dB rise from 4c to 6c and a 3.1 dB increase from 6c to 10c. These findings emphasize that there is an inverse relation between the increase in the receiver's distance and the increase in OASPL.

The findings presented in Fig. 10 provide a graphical representation of the relationship between noise generation and angle of attack. The figure illustrates the Overall Sound Pressure Level (OASPL) in all directions from a receiver positioned at a distance of 2c from the airfoil. This data highlights a clear correlation between the airfoil's aerodynamic noise and the angle of attack. Importantly, with an increasing angle of attack, OASPL proportionally rises.
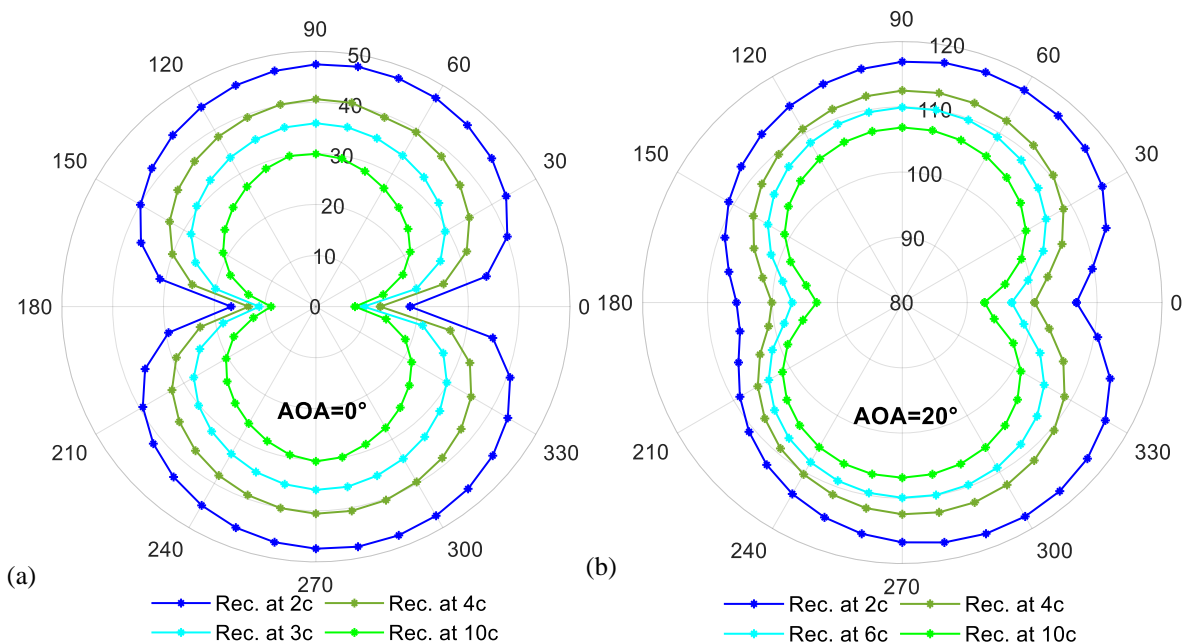

Fig. 9 Overall Sound pressure level at different receiver distances for: (a) AOA= 0° and (b) AOA= 20°
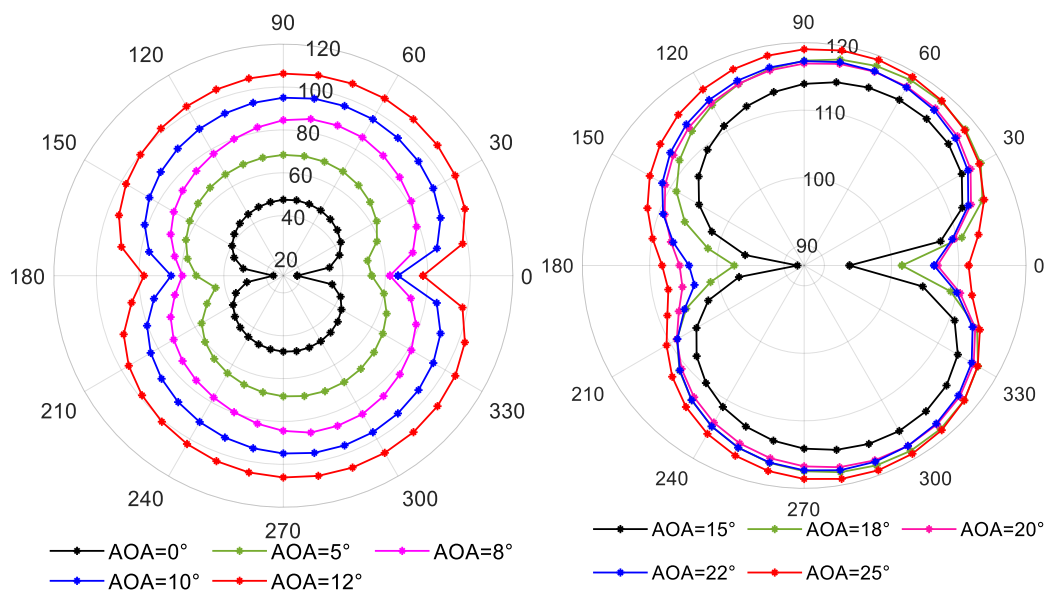
Fig. 10 Overall Sound pressure level at different angles of attack

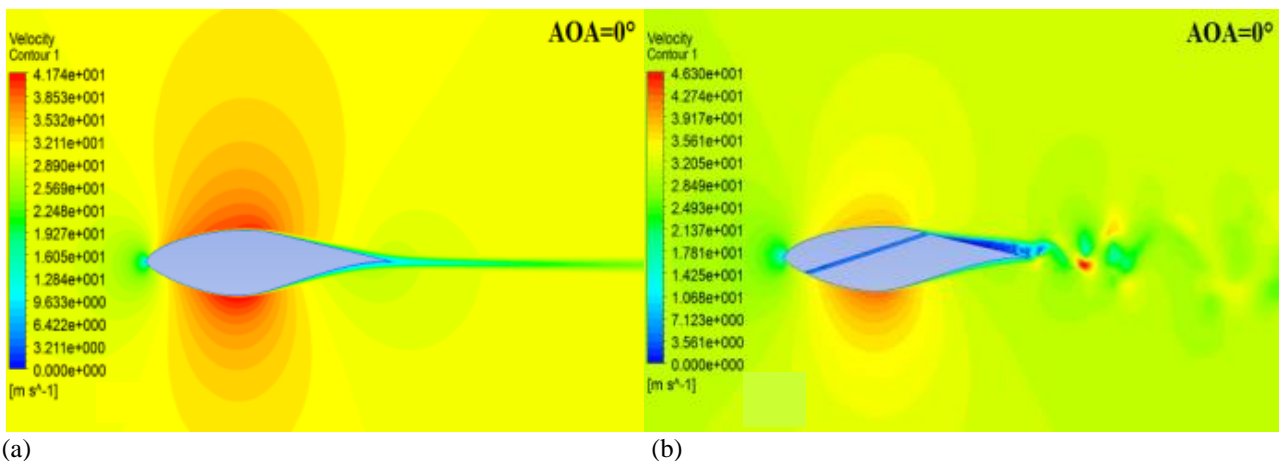(a)   (b)

Fig. 11 Velocity contour at AOA=0° for: (a) original airfoil (b) split airfoil

In the vertical direction (90°), there's a significant 71.59 dB increase in OASPL between AOA=0° and AOA=25°, primarily due to the boundary layer separation, which occurs as the angle of attack increases, resulting in the detachment of the boundary layer near the trailing edge. This leads to the upward movement of the separated region, giving rise to the generation of small counter-rotating vortices. Through interactions, these vortices contribute to the formation of a significant recirculation region, ultimately leading to detachment (stall phenomena). The stall noise is considered the dominant source of aeroacoustic noise compared to other sources.

4.4 Simulation Results

With the aim of controlling and reducing noise emissions from the airfoil, this study elucidates multiple scenarios, encompassing both controlled (split) and uncontrolled airfoil.

The observations at a zero angle of attack, depicted in Fig. 11, are consistent with the principles of laminar flow. At the stagnation point on the leading edge of the airfoil, where the airflow encounters the airfoil for the first time, the velocity is at its lowest. This is because the air particles slow down as they come into contact with the stationary surface of the airfoil. As the airflow continues along the surface of the airfoil towards the aft, the velocity gradually increases. This acceleration occurs as the air particles move along the streamlined shape of the airfoil, with the maximum velocity typically reached near the point of maximum thickness. However, as the airflow progresses further aft, it encounters adverse pressure gradients, causing the velocity to decrease. This adverse gradient leads to a reduction in velocity towards the trailing edge of the airfoil. When airflow is injected through the split in the airfoil, it brings in extra momentum to the flow. The premature flow separation changes the airflow pattern over the airfoil, affecting aerodynamic properties like lift and drag. It also impacts the generation of aerodynamic noise because the disrupted airflow interacts with the airfoil surface and nearby structures, potentially creating turbulent regions and vortices that contribute to noise.

Moreover, we can visualize the appearance of counter-rotating vortices downstream of the airfoil. This phenomenon elucidates the aerodynamic noise results at
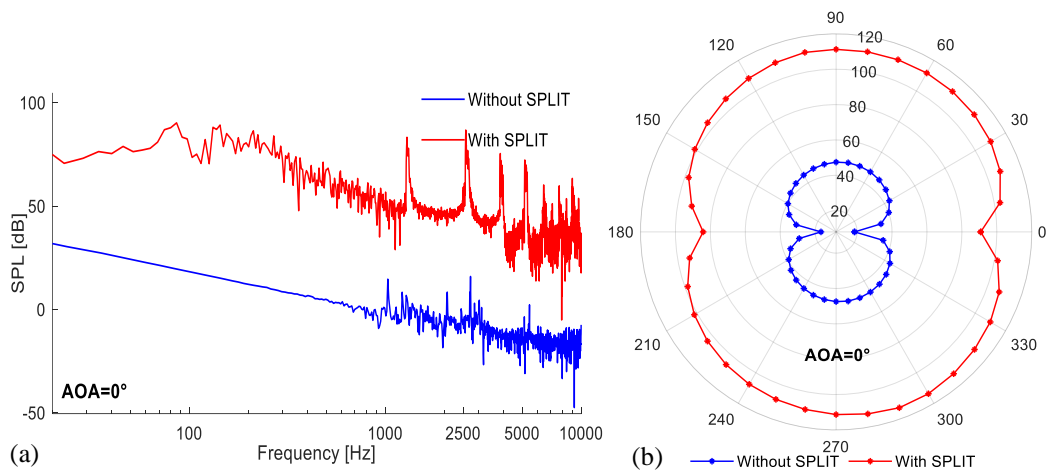
(a)   (b)

Fig. 12 Comparison of noise prediction between original airfoil and split Airfoil at AOA=0°: (a) Sound Pressure Level spectra (b) Overall Sound Pressure Level
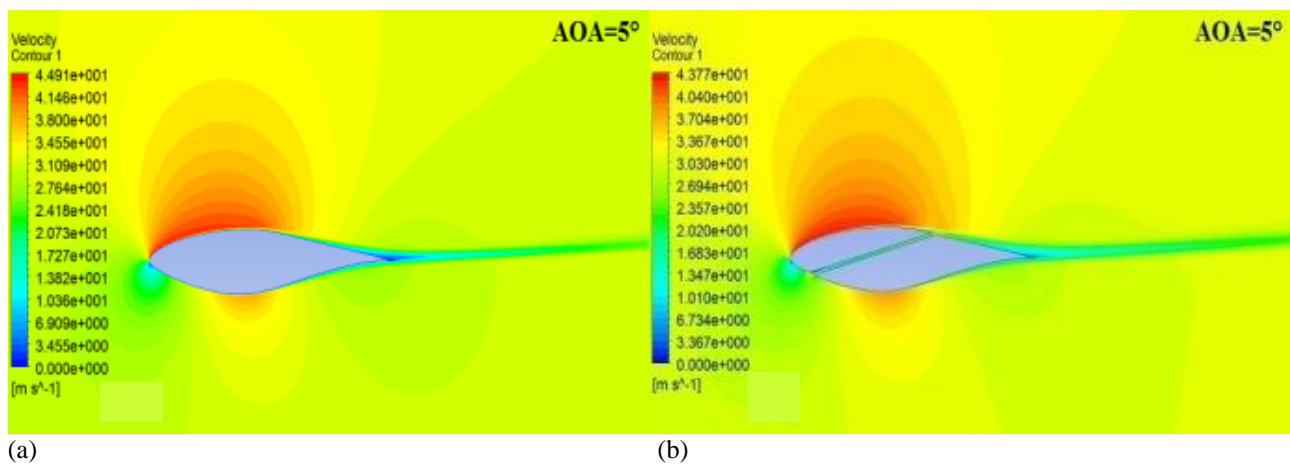

(a)   (b)

Fig. 13 Velocity contour at AOA= 5° for: (a) original airfoil (b) split airfoil

this angle, depicted in Fig. 12, where the noise emitted from the split airfoil surpasses that of the original profile. This difference represents a substantial increase of nearly six times. Additionally, we observe prominent peaks in the sound pressure level at frequencies exceeding 1000 Hz. Although these values align approximately with the frequencies of the original profile, they exhibit significantly higher sound pressure levels. The selected main frequencies - 1291 Hz, 2576 Hz, 3867 Hz, 5159 Hz, 6438 Hz, 7729 Hz, and 9014 Hz - correspond to SPL values of 83.31 dB, 86.81 dB, 75.45 dB, 72.33 dB, 60.26 dB, 59.83 dB, and 63.42 dB, respectively. Furthermore, there is a substantial elevation in the overall sound pressure level for the split airfoil, surpassing 63 dB in all directions.

An increase in the angle of attack disrupts the flow distribution over the original airfoil. At angles of attack less than 12° (AOA < 12°), the maximum velocity zone advances forward, and the stagnation point descends. The flow passing over the leading edge rapidly decelerates, leading to the formation of a small region of flow separation at the trailing edge (depicted in Fig. 13, Fig. 15, and Fig. 17 by a blue zone indicating zero velocity). However, the flow predominantly remains attached over

the majority of the airfoil's surface, maintaining a laminar boundary layer.

In the case of the split airfoil, the injected flow penetrates the separated zone and reaches the main flow, effectively reattaching the separated zone to the airfoil, creating a more stable layer and delaying the transition to turbulence. This, in turn, as shown in Figs. 14, 16, and 18, leads to a reduction in the aerodynamic noise generated by this zone.

Figure 16 illustrates that the sound pressure level produced by the profile with split at AOA=8° is notably lower than that of the original profile. This difference is particularly pronounced throughout the entire frequency spectrum, especially between 400 Hz and 1000 Hz, where the reduction is highly significant. Notably, we observe a distinct suppression of two prominent peaks corresponding to the frequencies of 416.7 Hz and 833.5 Hz, registering at 56.07 dB and 69.25 dB respectively.

Likewise, we also observe a considerable decrease for the split profile at AOA=10° (Fig. 18), greater than that at AOA=8°, by more than 25 dB for frequencies above 1500 Hz. Moreover, we notice a suppression of many significant peaks between 100 Hz and 1500 Hz, we highlight the highest values at 145 Hz, 309.9 Hz, and
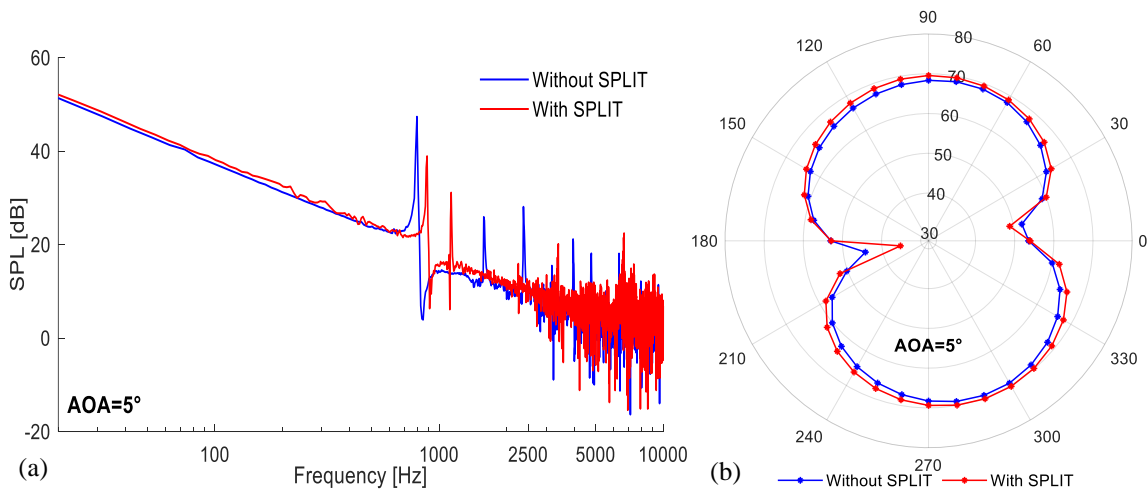
Fig. 14 Comparison of noise prediction between original airfoil and split Airfoil at AOA=5°: (a) Sound Pressure Level spectra (b) Overall Sound Pressure Level
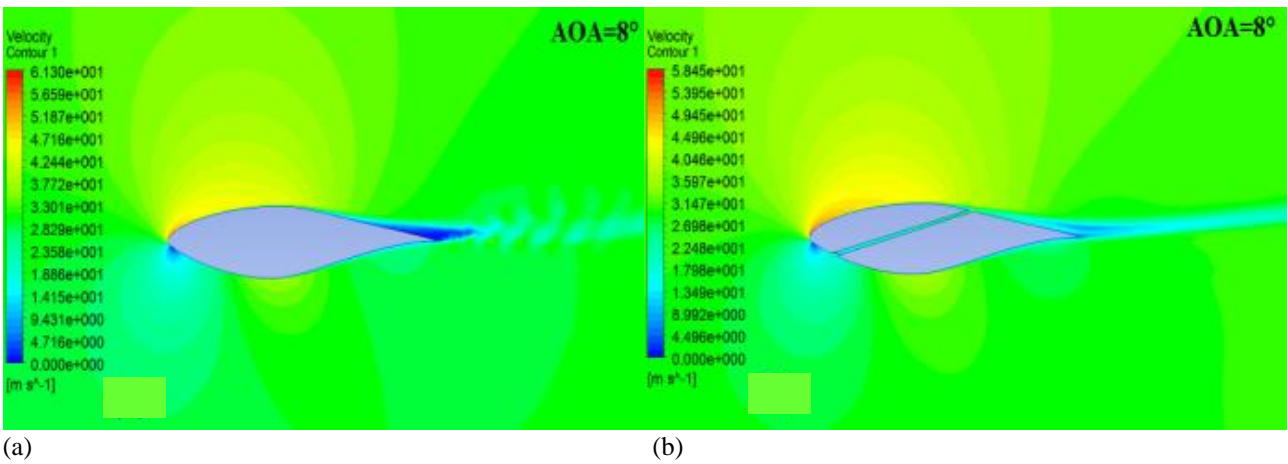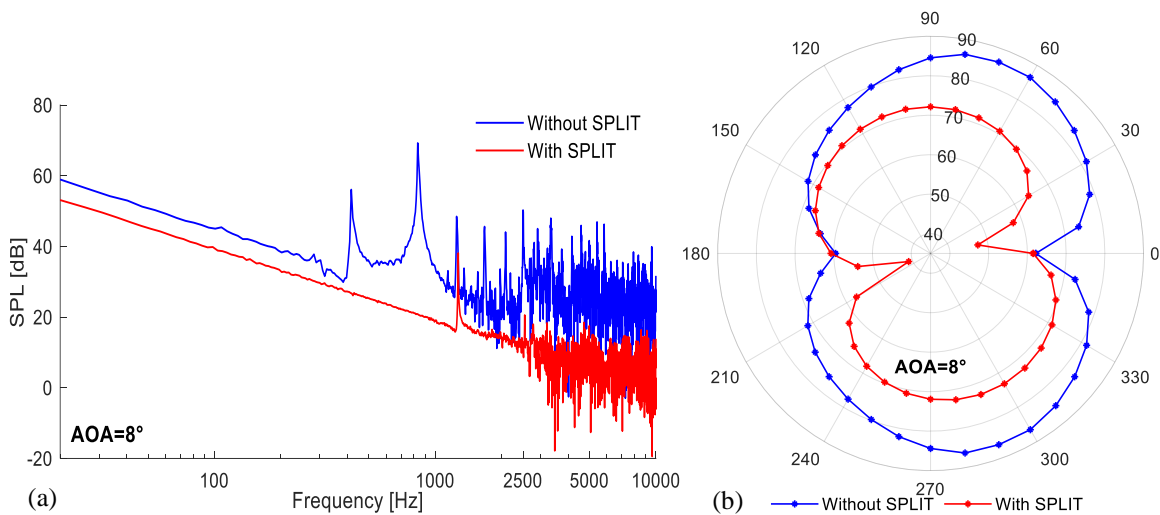

Fig. 15 Velocity contour at AOA=8° for: (a) original airfoil (b) split airfoil

Fig. 16 Comparison of noise prediction between original airfoil and split Airfoil at AOA=8°: (a) Sound Pressure Level spectra (b) Overall Sound Pressure Level

911.4 Hz, measuring 58.66 dB, 76.74 dB, and 69.87 dB, respectively.

Additionally, a considerable decrease in the overall sound pressure level is evident with the split airfoil at both AOA=8° and AOA=10°, surpassing 10 dB in the rear profile directions for AOA=8° and 30 dB in all directions for AOA=10°.
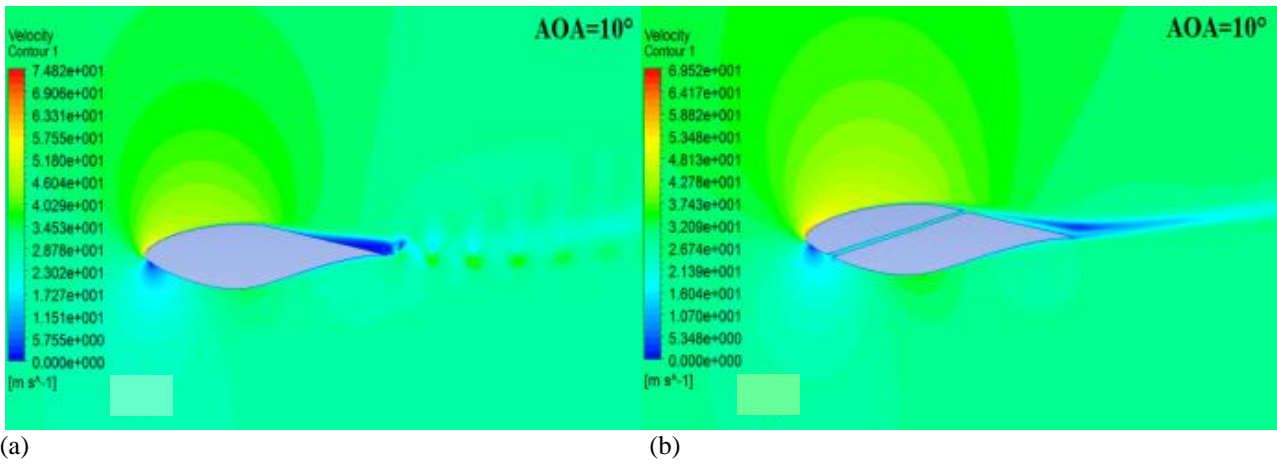
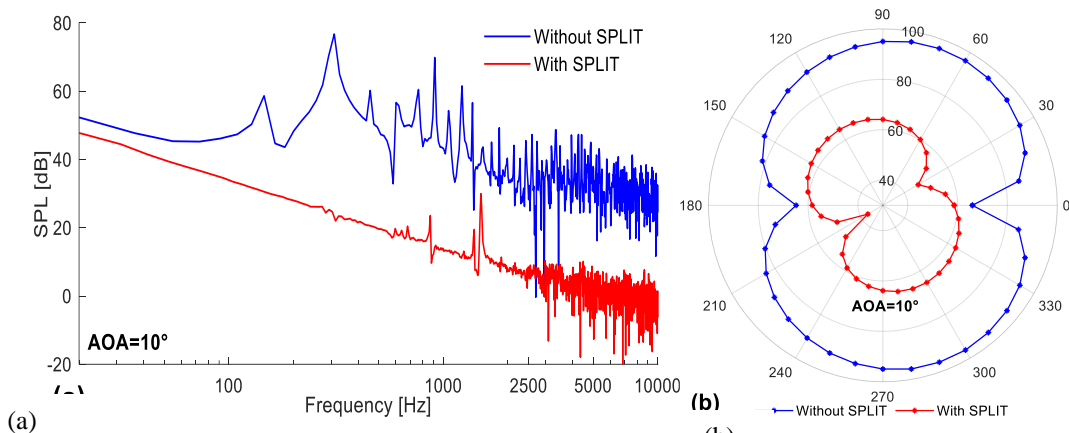**Fig. 17 Velocity contour at AOA=10° for: (a) original airfoil (b) split airfoil**

Fig. 18 Comparison of noise prediction between original airfoil and split Airfoil at AOA=10°: (a) Sound Pressure Level spectra (b) Overall Sound Pressure Level

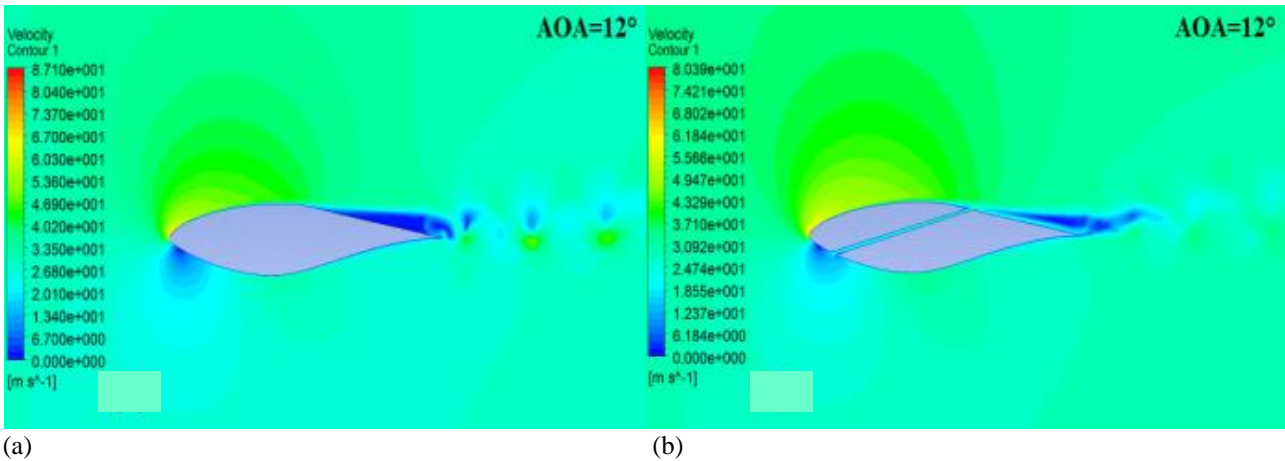**Fig. 19 Velocity contour at AOA=12° for: (a) original airfoil (b) split airfoil**

Small counter-rotating vortices begin forming downstream of the airfoil due to the flow separation zone and its interaction with the trailing edge (Fig. 19). As the angle of attack increases, the separation zone on the upper surface of the airfoil also expands and starts moving forward. Simultaneously, vortices begin to develop and interact, leading to increased aerodynamic noise. However, in the case of the split airfoil, the injected flow disrupts the separated zone, pushing the vortices away from the trailing edge (Fig. 21 and Fig.

23). This action contributes to reducing the noise generated.

Acoustic measurements conducted at moderate angles of attack reveal a substantial reduction in aerodynamic noise, particularly within frequencies below 1000 Hz. Figure 20 illustrates measurements at AOA=12°, clearly showing a marked reduction in sound pressure levels by up to 22 dB below 2500 Hz for the split profile. Additionally, there are significant reductions
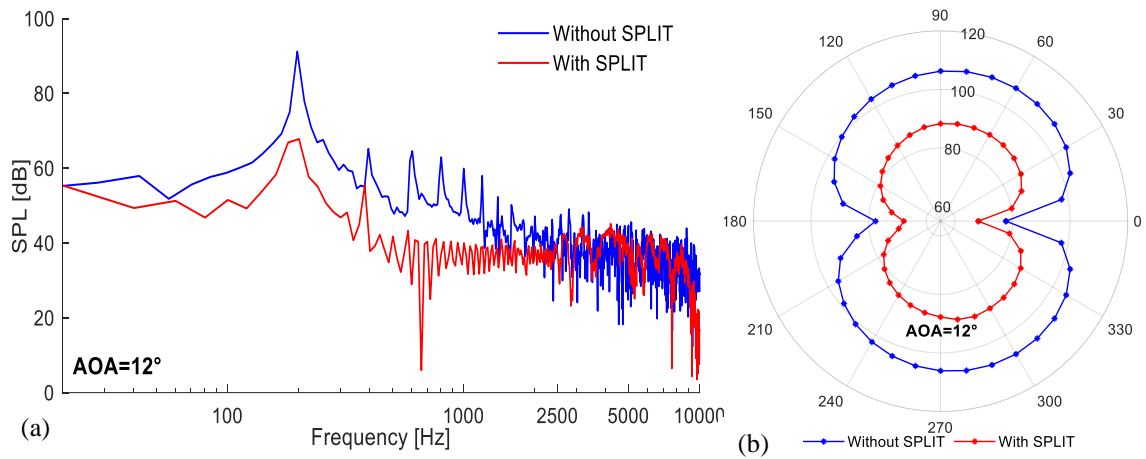
Fig. 20 Comparison of noise prediction between original airfoil and split Airfoil at AOA=12°: (a) Sound Pressure Level spectra (b) Overall Sound Pressure Level

Fig. 21 Velocity contour at AOA=15° for: (a) original airfoil (b) split airfoil

Fig. 22 Comparison of noise prediction between original airfoil and split Airfoil at AOA=15°: (a) Sound Pressure Level spectra (b) Overall Sound Pressure Level
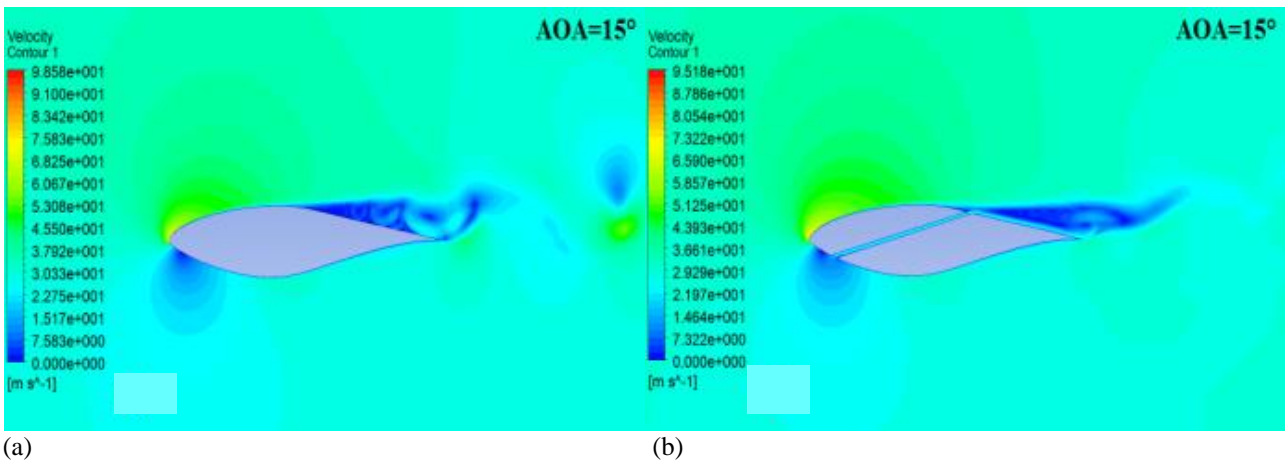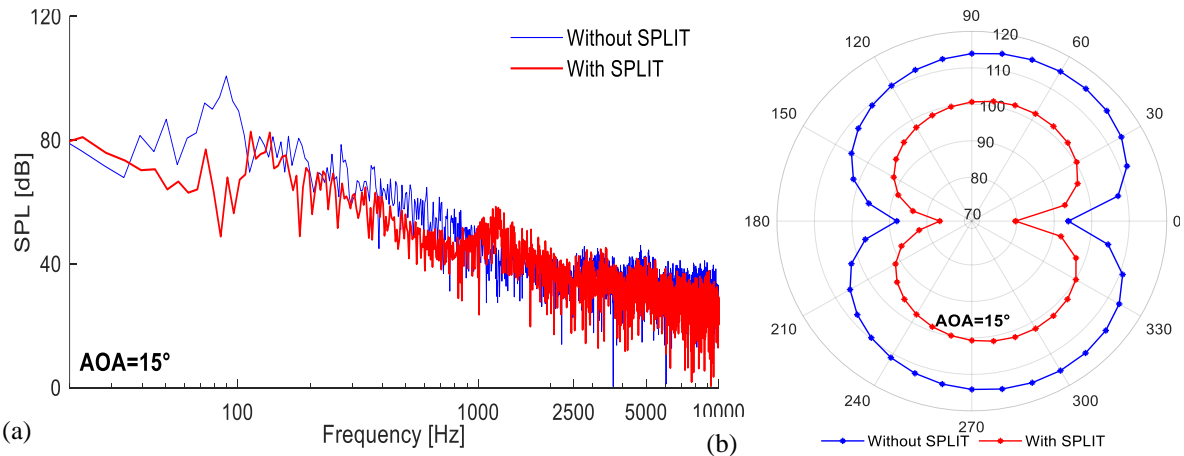
in peak values, reaching up to 20 dB. Furthermore, there is an important decrease of up to 18 dB in the overall sound pressure level across all directions.

Figure 22 displays measurements at AOA=15°, where we observe a reduction of approximately 9 dB between 150 Hz and 1000 Hz, and the suppression of a significant peak at 89.67 Hz, measuring 100.7 dB. There

is also a decrease of about 13 dB in the overall sound pressure level. These observations are continued in Fig. 24, which presenting acoustic measurements at 18°. Here, we observe a notable decrease at low frequencies, reaching up to 18 dB, and a decrease in the overall sound pressure level in all directions of about 12 dB.
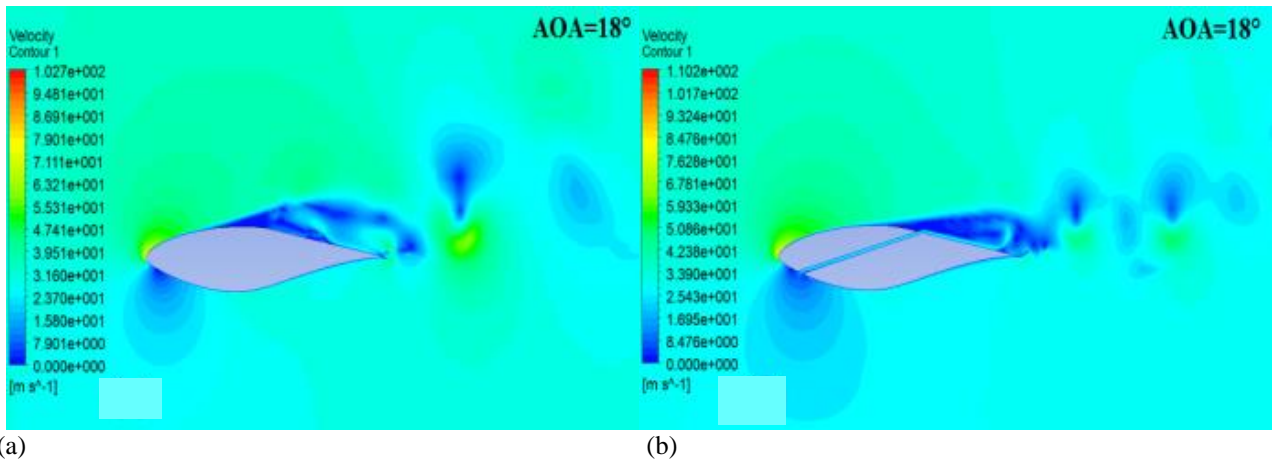
Fig. 23 Velocity contour at AOA=18° for: (a) original airfoil (b) split airfoil
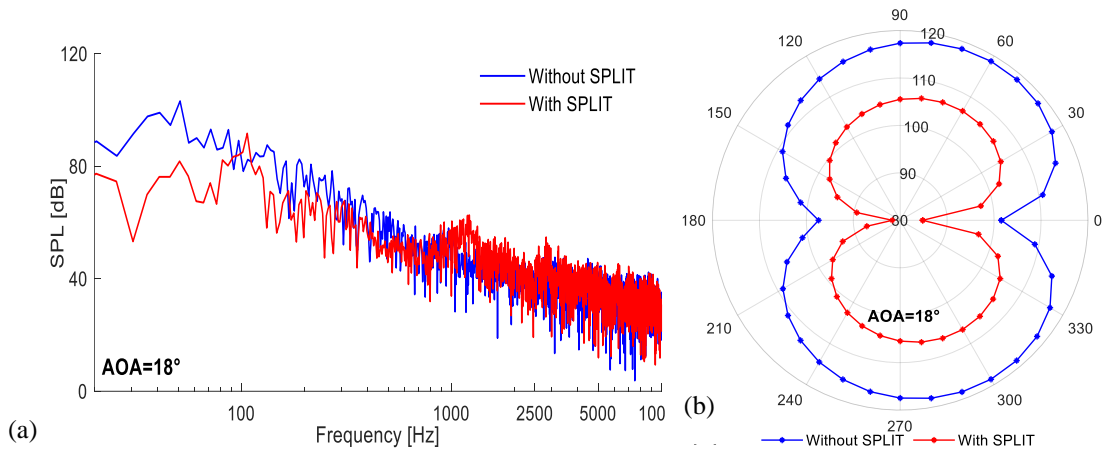

Fig. 24 Comparison of noise prediction between original airfoil and split Airfoil at AOA=18°: (a) Sound Pressure Level spectra (b) Overall Sound Pressure Level
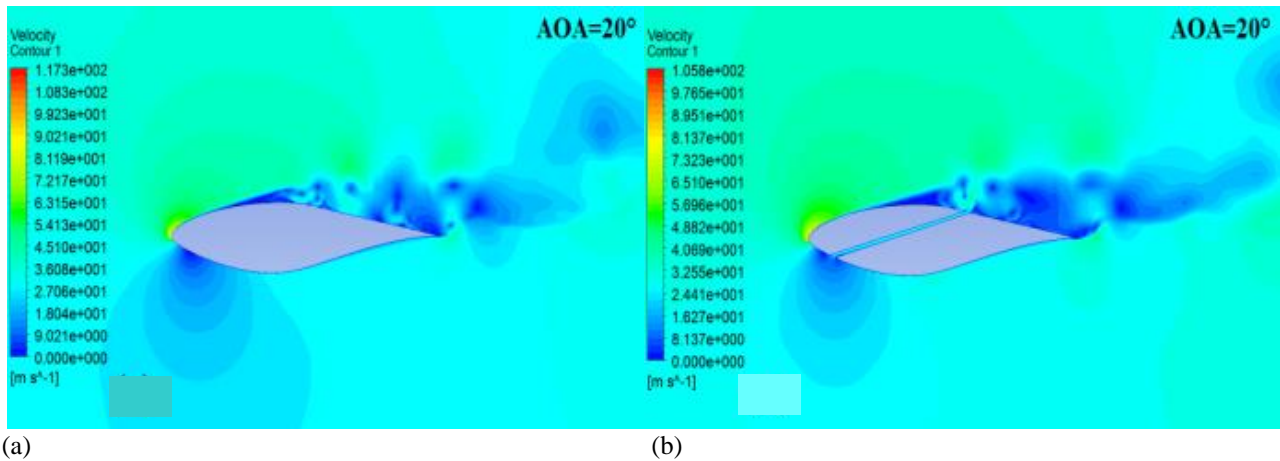

Fig. 25 Velocity contour at AOA= 20° for: (a) original airfoil (b) split airfoil

As the angle of attack (AOA) surpasses 18°, depicted in Figs 25 and 27, the upper surface boundary layer of the airfoil undergoes substantial detachment. This detachment is marked by the rapid forward movement of the transition point, which covers the suction side with small counter-rotating vortices. These vortices interact, fostering the formation of a significant recirculation region, a phenomenon that intensifies with increasing angle of attack. At high angles of attack, this extensive separation of airflow characterizes the airfoil's behavior, resulting in vigorous reversed airflow and ultimately inducing a stall condition, accompanied by intense aerodynamic noise generation. However, the positioning of a split on the airfoil can yield varying effects on the resulting aerodynamic noise, exemplified at AOA=20° (Fig. 26). Here, a notable reduction of approximately 4.5 dB in Overall Sound Pressure Level (OASPL) and a decrease of about 10 dB in Sound Pressure Level (SPL) for frequencies exceeding 200 Hz are observed. This reduction is attributed to the split's role in redirecting the flow, pushing vortices away from the trailing edge, thereby mitigating noise generation.

Fig. 26 Comparison of noise prediction between original airfoil and split Airfoil at AOA=20°: (a) Sound Pressure Level spectra (b) Overall Sound Pressure Level

Fig. 27 Velocity contour at AOA= 22° for: (a) original airfoil (b) split airfoil

Fig. 28 Comparison of noise prediction between original airfoil and split Airfoil at AOA=22°: (a) Sound Pressure Level spectra (b) Overall Sound Pressure Level

(a)   (b)

Fig. 29 Velocity contour at AOA= 25° for: (a) original airfoil (b) split airfoil

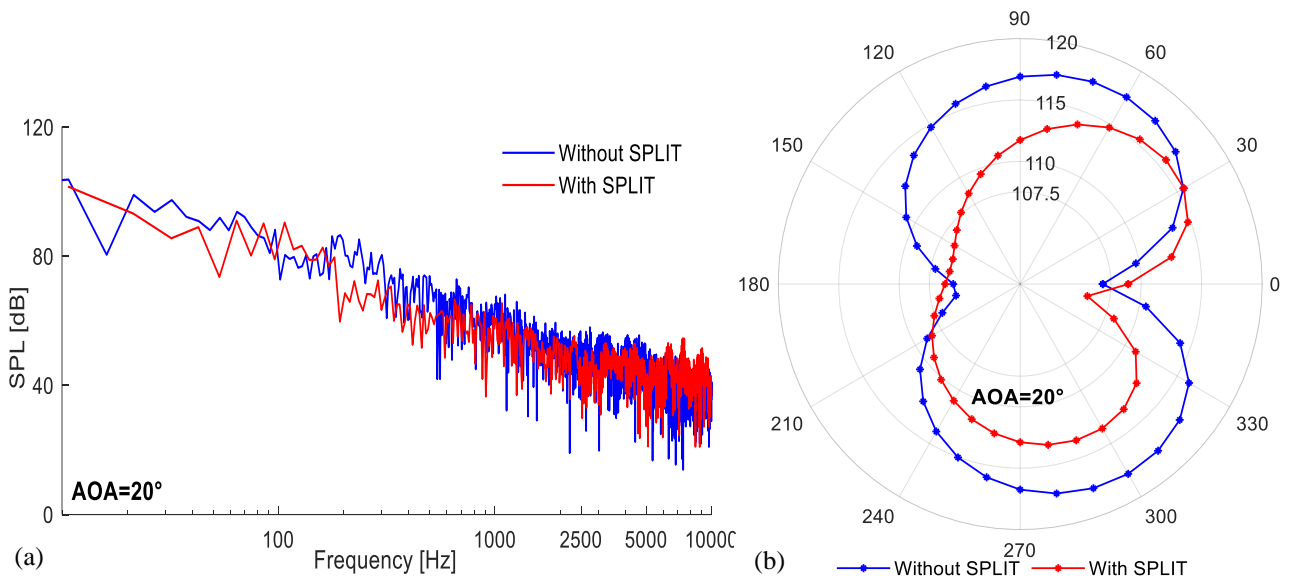(a)   (b)

Fig. 30 Comparison of noise prediction between original airfoil and split Airfoil at AOA=25°: (a) Sound Pressure Level spectra (b) Overall Sound Pressure Level
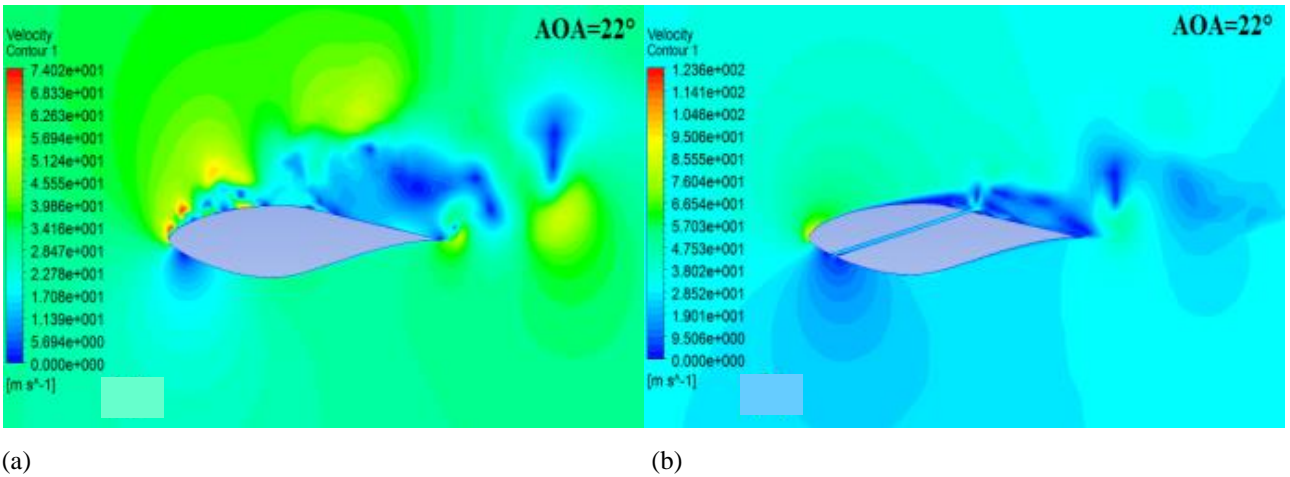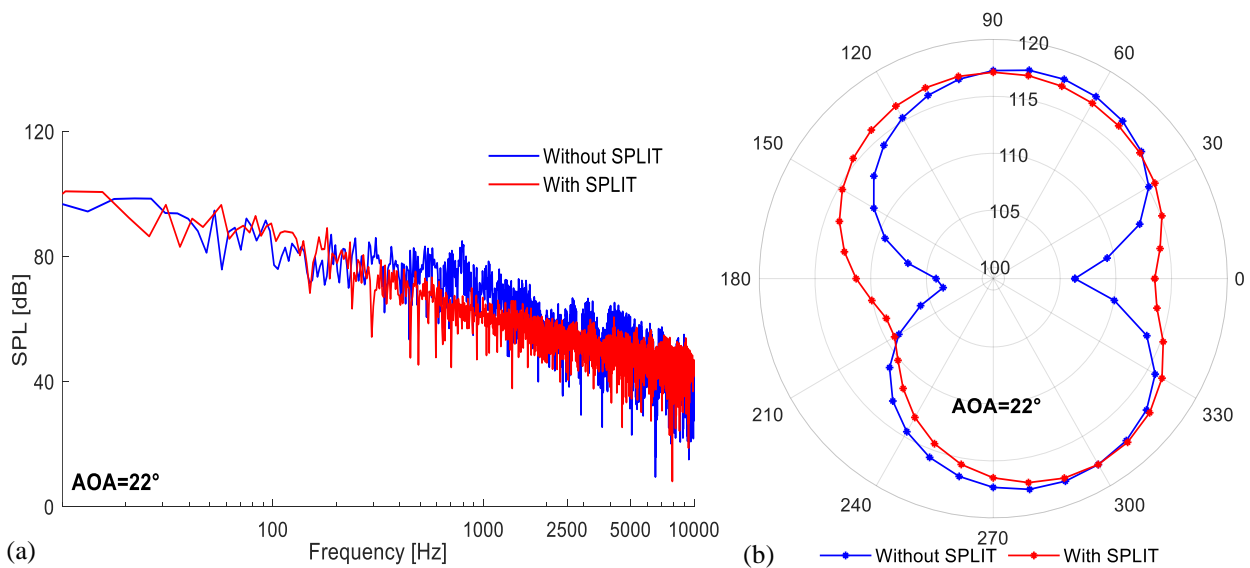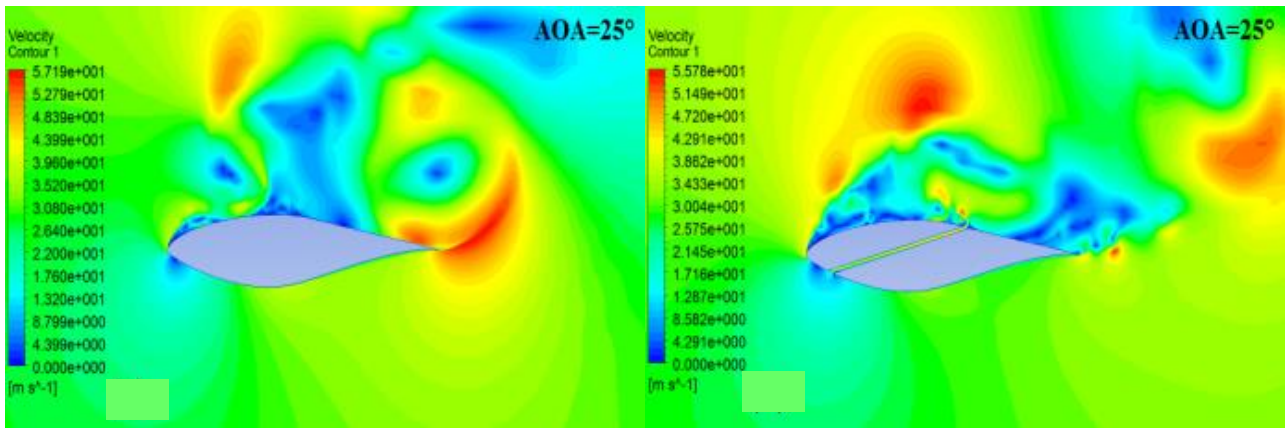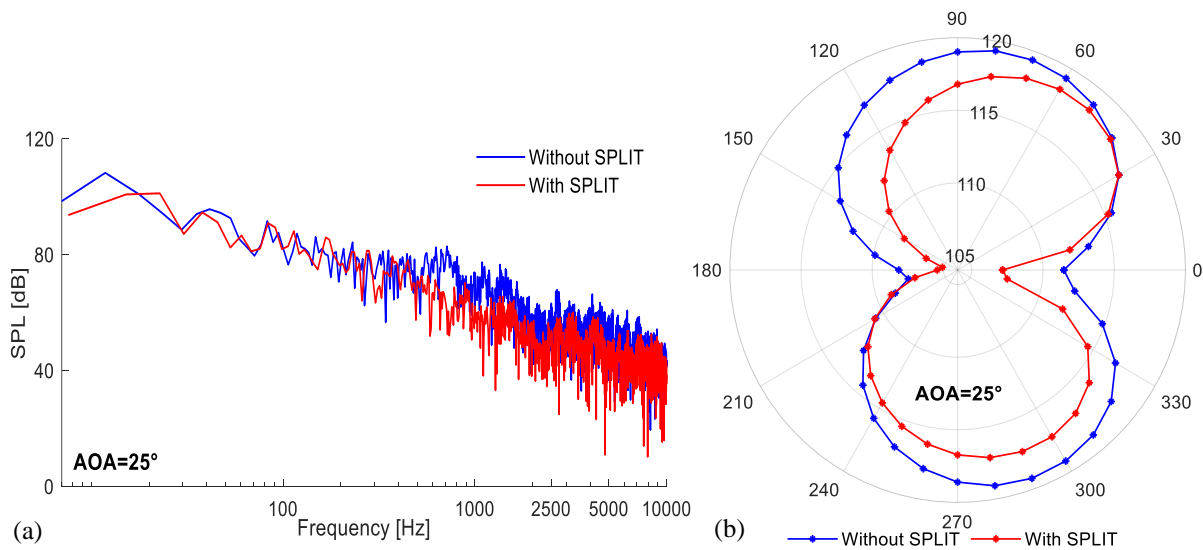
Conversely, at AOA=22° (Fig. 28), despite the split's ability to restore the laminar boundary layer near the leading edge (Fig. 27), a small increase in OASPL is noted (Fig. 28), although there is a slight decrease in SPL, estimated at 6 dB for frequencies greater than 500 Hz. With further increase in angle of attack to AOA=25° (Fig. 29), the upper surface boundary layer of the original airfoil completely detaches. On a split airfoil, the split outlet is positioned deep inside the separation zone, facilitating direct integration of the split's outgoing flow with the separated airflow. This integration imparts momentum to the flow in the direction of the primary airflow, weakening the reversed flow and fragmenting the separation region into smaller vortices. Consequently, there is a significant reduction in aerodynamic noise, with SPL above 500 Hz dropping by up to 15 dB and a noticeable 4 dB decrease in OASPL (Fig. 30).

5. CONCLUSION

This study investigates a passive control method employing a split airfoil to mitigate aerodynamic noise

resulting from boundary layer separation. At increasing angles of attack, the boundary layer detachment near the trailing edge leads to separation, causing the separated region to move upstream and generate small counter-rotating vortices. These vortices interact to form a substantial recirculation region before eventual detachment.

Aerodynamic performance was simulated using Delayed Detached-Eddy Simulation (DDES) based on the Spalart-Allmaras turbulence model. Simulations were conducted on an NREL S809 airfoil with and without a split configuration, maintaining a Reynolds number (Rec) of 1,000,000 based on the airfoil chord. Acoustic predictions were made using the Ffowcs Williams & Hawkings (FWH) acoustic analogy formulation. The study quantitatively analyzed velocity contours, Sound Pressure Level (SPL) distributions, and Overall Sound Pressure Level (OASPL) to assess the split's impact on aerodynamic performance and noise characteristics.

The findings of this study indicate that a substantial influence of aerodynamic noise is observed concerning

the angle of attack, underscoring a direct correlation between the increase in Overall Sound Pressure Level and the increase in the angle of attack. Furthermore, the results demonstrate a correlation between aerodynamic noise and the distance from the airfoil to the receiver, resulting in a reduction in sound pressure levels as this distance increases.

In the comparative analysis between the original airfoil and the split airfoil, the latter emerged as the more optimal configuration for noise reduction. We observed significant reductions in aerodynamic noise across various angles of attack, except for low angles (less than AOA=6°), where airflow injection through the split induced early flow separation, consequently elevating aerodynamic noise emissions. However, at intermediate angles of attack ranging from 6° to 18°, substantial reductions in aerodynamic noise were consistently observed. Notably, the Overall Sound Pressure Level demonstrated reductions of 14% at 8°, 16% at 10°, 19% at 12°, 13% at 15°, and 11% at 18°. Analysis of Sound Pressure Level revealed reductions of 12% at low frequencies and 60% at high frequencies for AOA=8°, 42% for AOA=10°, 35% for AOA=12°, 18% at low frequencies for AOA=15°, and 14% at frequencies exceeding 200Hz for AOA=18°.

For angles of attack surpassing AOA=18°, the impact of aerodynamic noise depended on the position of the split outlet relative to the separation zone. Notably, a reduction in Overall Sound Pressure Level (OASPL) was observed in nearly all directions for AOA=20° and AOA=25°, achieving reductions of 4.5% and 3%, respectively. However, at AOA=22°, a 5% increase in OASPL was noted only in certain directions, highlighting the sensitivity of noise reduction to the split outlet's positioning.

In other words, the comparative analyses between the original and split airfoils revealed that the split configuration consistently offers optimal noise reduction across a range of angles of attack. While the split occasionally resulted in increased noise levels at low angles (below AOA=6°), it predominantly yielded significant noise reductions at intermediate angles (6° to 18°) and beyond.

These findings represent a significant advancement in the field by showcasing the effectiveness of split airfoil designs in noise control. The practical implications of this study are far-reaching, extending to the design and optimization of quieter and more efficient airfoil structures, with potential applications in wind energy sectors. By deepening our understanding of the intricate relationship between aerodynamic performance and noise emissions, this research sets the stage for future investigations aimed at refining airfoil designs for enhanced acoustic performance and improved aerodynamic efficiency.

ACKNOWLEDGEMENTS

CONFLICT OF INTEREST

The authors declare that they have no financial or non-financial conflicts of interest pertaining to this research.

AUTHORS CONTRIBUTION

S. Khenfous carried out the numerical analyses, software development, data curation, and writing of the original draft. **M. Maizi** contributed to problem identification, methodology, and manuscript preparation. **M. Zamoum** assisted with supervision and validation.

REFERENCES

Acarer, S. (2020). Peak lift-to-drag ratio enhancement of the DU12W262 airfoil by passive flow control and its impact on horizontal and vertical axis wind turbines. *Energy*, *201*, 117659. https://doi.org/10.1016/j.energy.2020.117659

Ackermann, T., & Söder, L. (2000). Wind energy technology and current status: a review. *Renewable and sustainable energy reviews*, *4*(4), 315-374. https://doi.org/10.1016/S1364-0321(00)00004-6

Anicic, O., Petković, D., & Cvetkovic, S. (2016). Evaluation of wind turbine noise by soft computing methodologies: A comparative study. *Renewable and Sustainable Energy Reviews*, *56*, 1122-1128. https://doi.org/10.1016/j.rser.2015.12.028

Ansys, A. (2013). Fluent solver theory guide. *ANSYS, Inc*. Release 15.0, Southpointe. https://www.academia.edu/33546431/ANSYS_Fluent_Theory_Guide

Beyhaghi, S., & Amano, R. S. (2017). Improvement of aerodynamic performance of cambered airfoils using leading-edge slots. *Journal of Energy Resources Technology*, *139*(5), 051204. https://doi.org/10.1115/1.4036047

Beyhaghi, S., & Amano, R. S. (2018). A parametric study on leading-edge slots used on wind turbine airfoils at various angles of attack. *Journal of Wind Engineering and Industrial Aerodynamics*, *175*, 43-52. https://doi.org/10.1016/j.jweia.2018.01.007

Brentner, K. S., & Farassat, F. (1998). Analytical comparison of the acoustic analogy and Kirchhoff formulation for moving surfaces. *AIAA journal*, *36*(8), 1379-1386. https://doi.org/10.2514/2.558

Devenport, W., Burdisso, R. A., Camargo, H., Crede, E., Remillieux, M., Rasnick, M., & Van Seeters, P. (2010). Aeroacoustic testing of wind turbine airfoils. *National Renewable Energy Laboratory (NREL), Blacksburg, Virginia*. https://www.academia.edu/download/30805444/43471.pdf

Lighthill, M. J. (1952). On sound generated aerodynamically I. General theory. *Proceedings of*

the *Royal Society of London. Series A. Mathematical and Physical Sciences*, *211*(1107), 564-587. https://doi.org/10.1098/rspa.1952.0060

Liu, Q., Miao, W., Li, C., Hao, W., Zhu, H., & Deng, Y. (2019). Effects of trailing-edge movable flap on aerodynamic performance and noise characteristics of VAWT. *Energy*, *189*, 116271. https://doi.org/10.1016/j.energy.2019.116271

Liu, W. Y. (2017). A review on wind turbine noise mechanism and de-noising techniques. *Renewable Energy*, *108*, 311-320. https://doi.org/10.1016/j.renene.2017.02.034

Luo, K., Zhang, S., Gao, Z., Wang, J., Zhang, L., Yuan, R., Fan, J., & Cen, K. (2015). Large-eddy simulation and wind-tunnel measurement of aerodynamics and aeroacoustics of a horizontal-axis wind turbine. *Renewable Energy*, *77*, 351-362. http://dx.doi.org/10.1016/j.renene.2014.12.024

Maizi, M., Dizene, R., & Mihoubi, M. C. (2017). Reducing noise generated from a wind turbine blade by pitch angle control using CFD and acoustic analogy. *Journal of Applied Fluid Mechanics*, *10*(4), 1201-1209. https://doi.org/10.18869/acadpub.jafm.73.241.27426

Maizi, M., Mohamed, M. H., Dizene, R., & Mihoubi, M. C. (2018). Noise reduction of a horizontal wind turbine using different blade shapes. *Renewable Energy*, *117*, 242-256. https://doi.org/10.1016/j.renene.2017.10.058

Mo, J. O., & Lee, Y. H. (2011). Numerical simulation for prediction of aerodynamic noise characteristics on a HAWT of NREL phase VI. *Journal of Mechanical Science and Technology*, *25*, 1341-1349. https://doi.org/10.1007/s12206-011-0234-1

Mohamed, M. H. (2014). Aero-acoustics noise evaluation of H-rotor Darrieus wind turbines. *Energy*, *65*, 596-604. https://doi.org/10.1016/j.energy.2013.11.031

Mohamed, M. H. (2019). Criticism study of J-Shaped darrieus wind turbine: Performance evaluation and noise generation assessment. *Energy*, S0360-5442(19)30735-2. https://doi.org/10.1016/j.energy.2019.04.102

Mohamed, M. H. (2021). Synergistic analysis of the aerodynamic impact of a new design of darrieus wind turbine. *Energy Sources, Part A: Recovery, Utilization, and Environmental Effects*, 1-20. https://doi.org/10.1080/15567036.2021.1900953

Moshfeghi, M., & Hur, N. (2020). Power generation enhancement in a horizontal axis wind turbine blade using split blades. *Journal of Wind Engineering and Industrial Aerodynamics*, *206*, 104352. https://doi.org/10.1016/j.jweia.2020.104352

Moshfeghi, M., Ramezani, M., & Hur, N. (2021). Design and aerodynamic performance analysis of a finite span double-split S809 configuration for passive flow control in wind turbines and comparison with single-split geometries. *Journal of Wind Engineering and Industrial Aerodynamics*, *214*, 104654. https://doi.org/10.1016/j.jweia.2021.104654

Moshfeghi, M., Shams, S., & Hur, N. (2017). Aerodynamic performance enhancement analysis of horizontal axis wind turbines using a passive flow control method via split blade. *Journal of Wind Engineering and Industrial Aerodynamics*, *167*, 148-159. http://dx.doi.org/10.1016/j.jweia.2017.04.001

Somers, D. M. (1997). *Design and experimental results for the S809 airfoil* (No. NREL/SR-440-6918). National Renewable Energy Lab.(NREL), Golden, CO (United States). https://www.nrel.gov/docs/legosti/old/6918.pdf

Spalart, P. R. (2000). Strategies for turbulence modelling and simulations. *International Journal of Heat and Fluid Flow*, 21(3), 252-263. https://doi.org/10.1016/S0142-727X(00)00007-2

Spalart, P. R., & Allmaras, S. (1992). *A one-equation turbulence model for aerodynamic flows.* 30th aerospace sciences meeting and exhibit (p. 439). https://doi.org/10.2514/6.1992-439

Spalart, P. R., Deck, S., Shur, M. L., Squires, K. D., Strelets, M. K., & Travin, A. (2006). A new version of detached-eddy simulation, resistant to ambiguous grid densities. *Theoretical and Computational Fluid Dynamics*, *20*, 181-195. https://doi.org/10.1007/s00162-006-0015-0

Su, J., Lei, H., Zhou, D., Han, Z., Bao, Y., Zhu, H., & Zhou, L. (2019). Aerodynamic noise assessment for a vertical axis wind turbine using improved delayed detached eddy simulation. *Renewable Energy*, *141*, 559-569. https://doi.org/10.1016/j.renene.2019.04.038

Wasala, S. H., Storey, R. C., Norris, S. E., & Cater, J. E. (2015). Aeroacoustic noise prediction for wind turbines using Large Eddy Simulation. *Journal of Wind Engineering and Industrial Aerodynamics*, *145*, 17-29. http://dx.doi.org/10.1016/j.jweia.2015.05.011

Williams, J. F., & Hawkings, D. L. (1969). Sound generation by turbulence and surfaces in arbitrary motion. *Philosophical Transactions for the Royal Society of London. Series A, Mathematical and Physical Sciences*, 321-342. https://doi.org/10.1098/rsta.1969.0031